

Crustal-scale transport of nanoparticle emulsion forms ore deposits

Laura Petrella (✉ laura.petrella@uwa.edu.au)

University of Western Australia

Nicolas Thebaud

University of Western Australia

Denis Fougerouse

Curtin University <https://orcid.org/0000-0003-3346-1121>

Laure Martin

RSES/ANU

Stephen Turner

Newmont Corporation

Alexandra Suvorova

University of Western Australia

Sarah Gain

Geological Survey of Western Australia

Article

Keywords: economic metal deposits, metal nanoparticles, metalliferous deposit formation

Posted Date: August 27th, 2021

DOI: <https://doi.org/10.21203/rs.3.rs-669530/v1>

License:  This work is licensed under a Creative Commons Attribution 4.0 International License.

[Read Full License](#)

Version of Record: A version of this preprint was published at Nature Communications on July 1st, 2022.

See the published version at <https://doi.org/10.1038/s41467-022-31447-5>.

1 Crustal-scale transport of nanoparticle emulsion forms ore
2 deposits

3 **Laura Petrella^{1*}, Nicolas Thébaud¹, Denis Fougerouse², Laure Martin³, Stephen
4 Turner⁴, Alexandra Suvorova³, Sarah Gain⁵**

5

6 ¹Centre for Exploration Targeting, University of Western Australia, Crawley 6009, Australia

7 ²School of Earth and Planetary Sciences, Curtin University, Bentley 6102, Australia

8 ³Centre for Microscopy Characterisation and Analysis, The University of Western Australia, Perth,
9 Western Australia, Australia

10 ⁴Newmont Corporation, Welshpool, WA 6106, Australia

11 ⁵Geological Survey of Western Australia, Perth, Western Australia, Australia

12

13 *Corresponding author: laura.petrella@uwa.edu.au

14

15 **ABSTRACT**

16 A 10- to 10 000-fold enrichment is required to form economic metal deposits. Such enrichment is
17 achieved through the accumulation of metals transported in hydrothermal fluids from their source
18 to the deposit. The contribution of gold nanoparticle suspensions in fluids is required to form
19 bonanza gold grades. However, as the source of gold is spatially disconnected from the deposit
20 location, it is not known how the transport of gold nanoparticles is achieved. Here we show that
21 metal nanoparticles (Au, AgO, AuAg Cu) are stabilised by colloidal silica in nanoparticle emulsion and
22 transported with the aid of low-density carbonic phases. We document systematic occurrence of
23 metals nanoparticle in five deposits that show a previously unrecognized association with
24 amorphous silica and carbon. Our results demonstrate that stabilisation of metal nanoparticles may
25 be achieved over kilometres through the Earth's upper crust and offers a step change in our
26 understanding of metalliferous deposit formation.

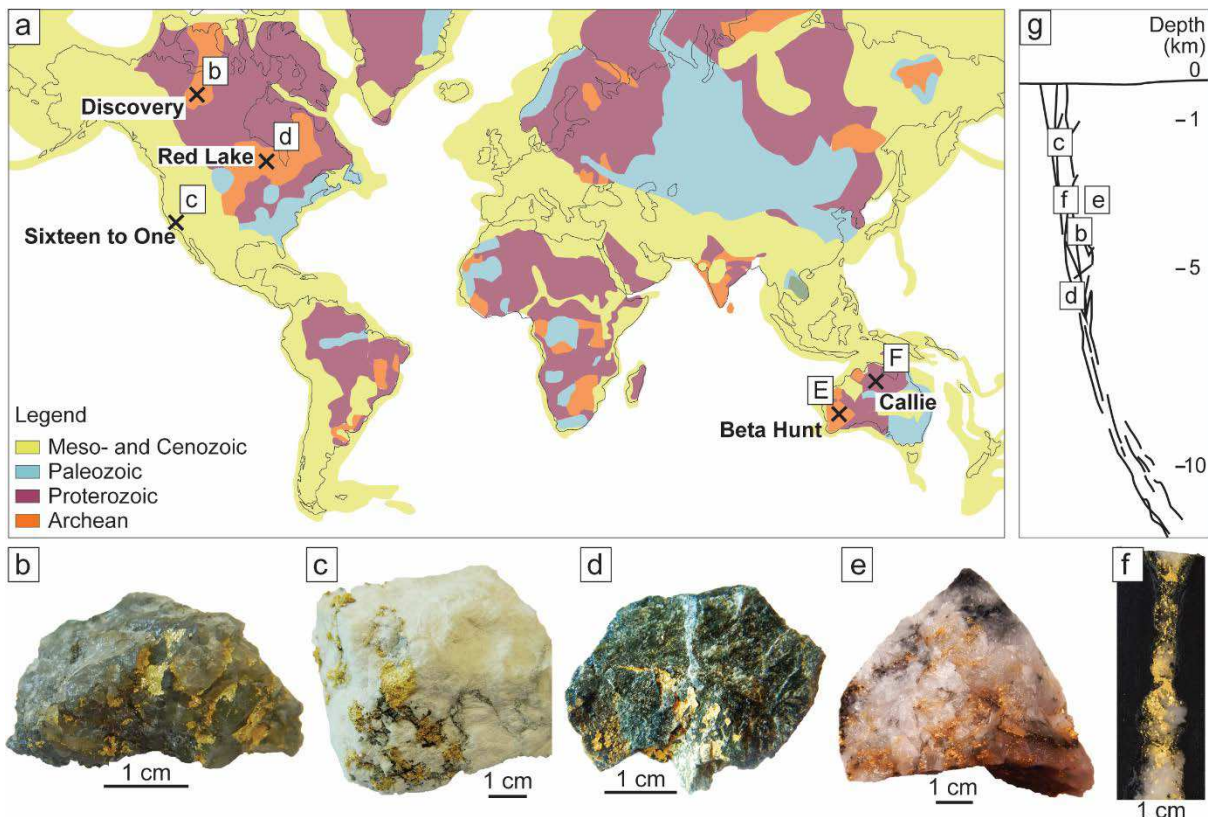
27

28 **INTRODUCTION**

29 Gold has played a critical role in the rise and collapse of human civilizations from the fifth
30 millennium BC in Egypt through to our modern era¹. This rare transition metal, of unique properties,
31 is generally extracted from mineral deposits that formed through the circulation of gold-bearing
32 aqueous solutions in the Earth's interior². Orogenic-type gold deposits, which account for over 75%
33 of the world's gold production³, often form very high-grade gold-rich quartz-carbonate veins. The
34 presence of high grades within orogenic gold deposits is a critical advantage, when compared to low-
35 grade and high tonnage deposits, as it provides a more valuable and sustainable resource due to
36 increased extraction efficiency and lesser environmental footprint.

37 Orogenic gold deposits form within the upper crust, in metamorphic belts, through a network of
38 veins and faults which transmit deeply sourced aqueous solutions^{4,5}. In most orogenic-type gold
39 deposits, the mineralising aqueous fluids are characterized by temperatures ranging from ~250 to

40 450°C, pressures from 500 to 1500 bars, low salinities, high CO₂ and H₂S content and a near neutral
41 pH⁶. From their deeply sourced reservoir(s) to the deposit site and at the above stated conditions,
42 gold is assumed to be most stable under the form of a dissolved complex⁷. The formation of
43 extremely high-grade gold mineralisation (~10,000 ppm Au) that is often observed in narrow (few
44 mm to cm) quartz veins⁸ is difficult to reconcile with the destabilisation of dissolved gold complexes
45 that can only achieve low solubilities (in the ppb range⁹) in hydrothermal solutions^{7,10}. Therefore,
46 the general low metal solubility in aqueous solutions needs to be compensated to explain high-grade
47 mineralisation¹⁰. To address this long-standing dilemma, it was proposed that gold can be
48 transported as nanoparticles (NP) suspension in solutions¹¹⁻¹³. Gold NP suspensions can concentrate
49 up to ~5000 times more gold in solution than as a dissolved species¹⁴ and offers an interesting
50 alternative to metal transport in aqueous fluids. The evidence for NPs in orogenic gold systems is,
51 however, limited^{15,16} and makes their contribution to the total deposit gold budget questionable.
52 Moreover, the bulk of gold enrichment forms away from the metal source and it is not known how
53 nanoparticles can be stabilized and transported over crustal scales. The limited data available on the
54 stability of Au NP in crustal solutions does not permit to dismiss or confirm the possibility that
55 metals can be transported over several kilometres within the upper crust. This study presents a
56 possible mechanism associated with the transport of metal NP by investigating natural samples.
57 Gold-rich quartz vein samples were collected from five gold deposits characterized by locally high-
58 grade (up to 70% visible gold¹⁷) deposits that formed at crustal depths ranging from > 5 km to 1.5
59 km below the surface¹⁸⁻²². The deposits formed in different host lithologies and range from the
60 Archean to the Cretaceous^{8,23-27} (**Fig. 1**).



61

62 **Fig. 1: Sample's location and description.** **a.** Location of the deposits from which samples were collected for
 63 this study; the deposit locations are shown on a world map indicating the thermo-tectonic age of the country
 64 rocks, modified from USGS thermo-tectonic data²⁸. **b** to **f** show photographs of the gold-rich quartz vein
 65 specimen used in this study: **b**. Discovery sample; **c**. Sixteen to One sample; **d**. Red Lake sample; **e**. Beta Hunt
 66 sample; **f**. Callie sample. **g.** Schematic representation showing the variability in depth of formation for the
 67 deposits studied along a crustal-scale network of fractures and faults.

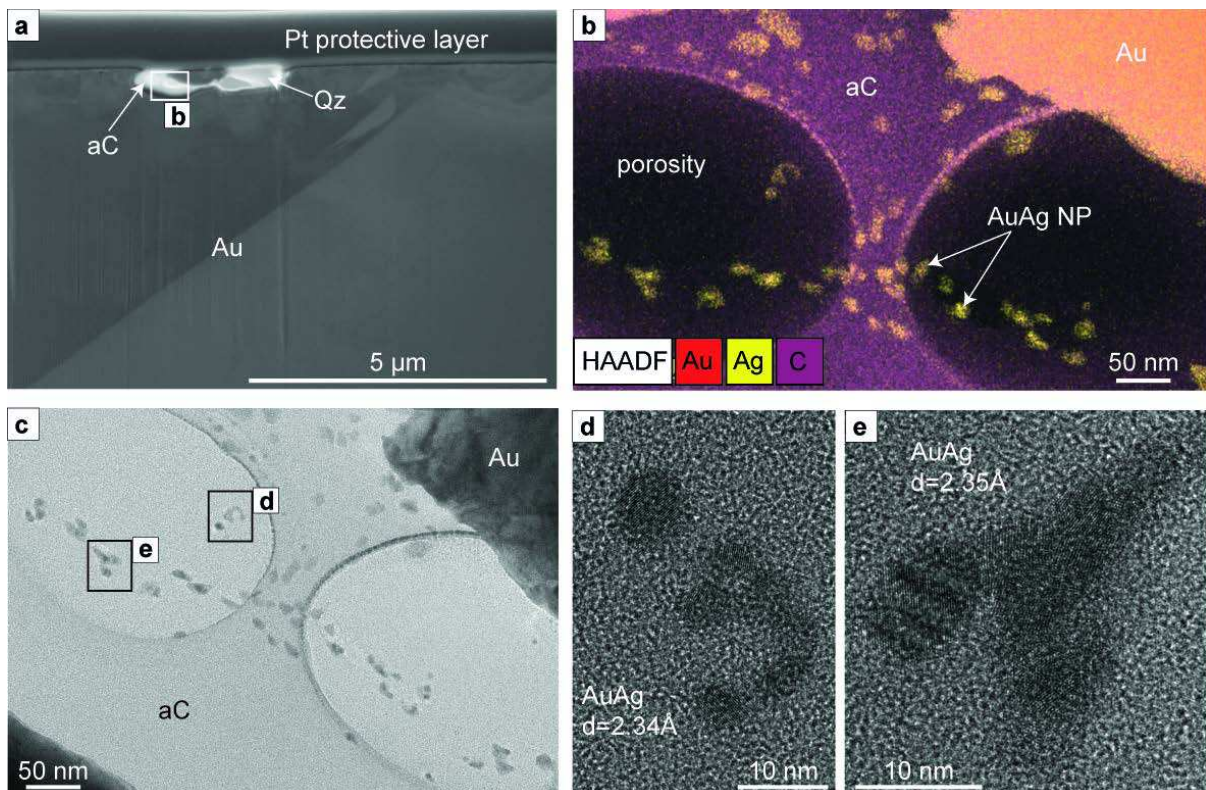
68

69 Results

70 Gold micro-inclusions and metal nanoparticles

71 **Red lake sample.** From the Red Lake sample, one foil was extracted from a gold grain which contains
 72 one ~3 µm elongated inclusion located close to the surface of the foil (**Fig. 2a**). Transmission
 73 electron microscope (TEM) analyses shows that the inclusion has two components: a quartz
 74 crystalline phase and an amorphous carbonic phase. The composition of the phases was confirmed
 75 by STEM EDS mapping (**Fig. 2b**). The crystallinity or absence of crystallinity was confirmed by FTT
 76 diffractograms acquired from both phases. The carbon amorphous phase preserves “bubble” like
 77 textures, these could correspond to porosity due to remnant fluid inclusions realized during foil
 78 preparation or they could be an artefact caused by inhomogeneous milling during the FIB

79 preparation process. The amorphous carbonic phase encapsulates numerous rounded nanoparticles
 80 that are locally aggregated to form various morphologies (**Fig. 2c to e**). The size of the nanoparticles
 81 varies from 2 nm (for single nanoparticles) to 20 nm (for the aggregate of several nanoparticles) as
 82 shown in **Fig. 2e**. The d-spacing of the nanoparticles varies between 2.34\AA and 2.35\AA indicative of Au
 83 (111) or Ag (111) or AuAg (111). Quantitative composition obtained by EDS on one NP indicate ~ 54
 84 at% Au, ~ 41 at% Ag and ~ 5 at% O (supplementary information), which indicate electrum.



85 **Fig. 2: Red Lake electrum nanoparticles in amorphous carbon.** **a**, TEM image of the Red Lake foil showing the
 86 elongated inclusion at the surface of the foil that is mainly composed of quartz (Qz) and an amorphous
 87 carbonic-phase (aC), the rest of the foil comprises coarse gold including two grains of different crystal
 88 orientation, the foil is covered by a platinum (Pt) protective layer at the top of the foil; **b**, EDS element map
 89 overlaying a High-Angle Annular Dark Field (HAADF) image from the middle of the inclusion and indicated in a
 90 white rectangle in Fig 2a. The figure shows the presence of electrum NP encapsulated in a carbon-rich phase; **c**,
 91 TEM image of the area shown in a white rectangle in Fig 2a. The inclusion is composed of amorphous material
 92 that is mainly carbon (light grey) and NPs that are the darker grey sub-rounded features within the amorphous
 93 material. The two large, “bubble”-like features in the image correspond to cavities within the amorphous
 94 phase, the cavities may have formed during the thinning of the foil. The absence of atomic arrangement within
 95 the carbon phase was confirmed by a diffractogram obtained in the lower part of the image avoiding the NP; **d**
 96 and **e**, High Resolution TEM (HRTEM) image of the areas shown in black rectangles in Fig 2c. showing electrum
 97 NPs with sizes varying between 4 nm to 10 nm in diameter. The diffractogram collected over the largest NP
 98 confirms a d-spacing of 2.34 that corresponds to Ag and/or Au.

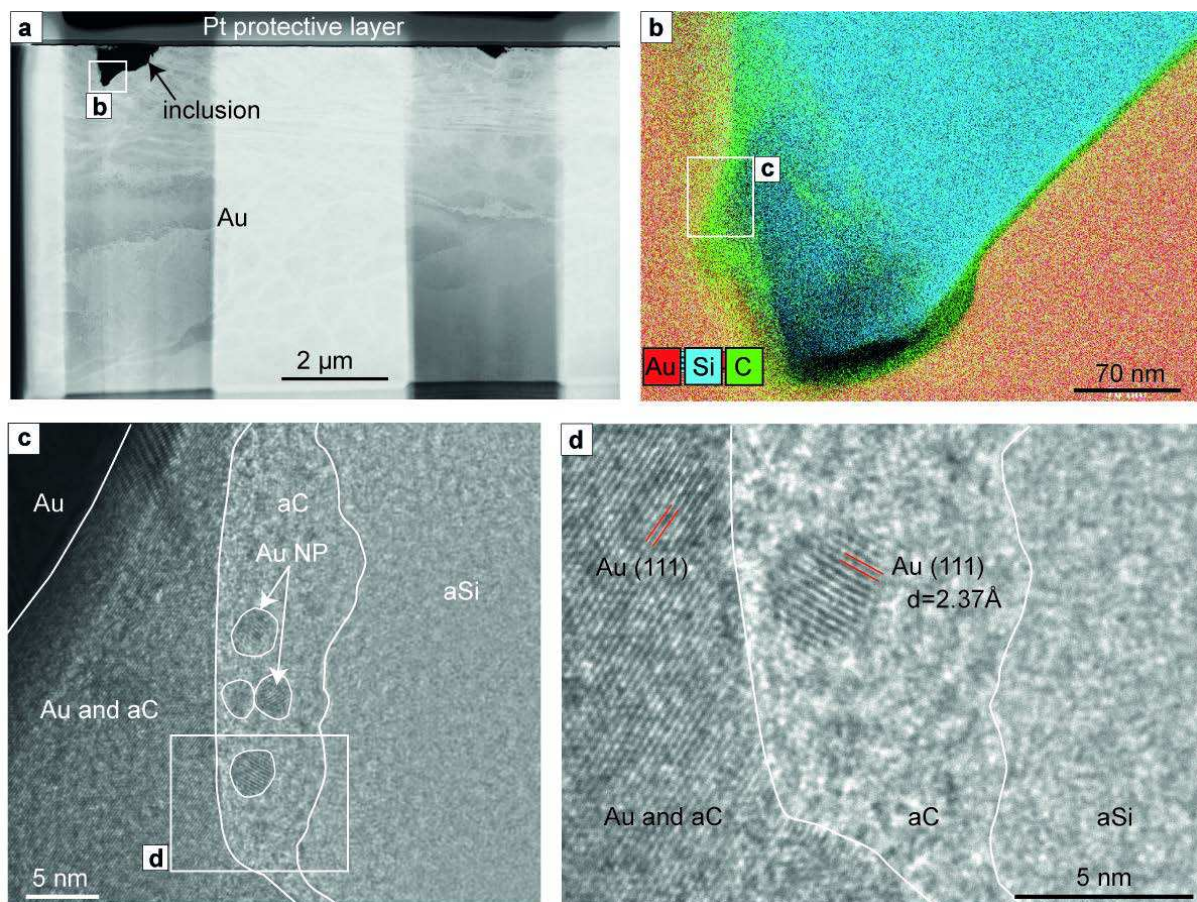
101 **Beta Hunt.** One foil extracted from a gold grain of the Beta Hunt sample contains one inclusion that
102 is c. 1.5 μm in diameter (**Fig. 3a**) and is composed of two phases: a homogeneous silica phase that
103 occupies the middle part of the inclusion and a thinner, homogeneous carbonic phase located over a
104 fine area along the edge of the inclusion (**Fig. 3b**). HRTEM image does not show any crystalline
105 features within both phases and FFT diffractogram from both areas confirming that the phases are
106 amorphous. As the TEM image is a projection through the entire thickness of the sample, in some
107 areas the various phases might overlap (**Fig. 3c**). Rounded gold or silver NP were observed in the
108 amorphous carbonic phase (**Fig. 3c, b**). The NP are very small (3 to 5 nm) and concentrated within a
109 thin sliver of amorphous carbonic phase near the contact with the gold crystal. A d-spacing of 2.37 \AA
110 was measured for the NP indicating a gold or silver composition for the crystal orientation of (111).
111 Due to the small size of the NPs, the EDS signal was not sufficient to determine whether they were
112 composed of Au, Ag or an Au-Ag alloy such as electrum. Other gold NP were observed in the
113 amorphous silica phase within the upper part of the inclusion (supplementary information).

114

115 **Discovery.** Two foils were extracted in gold grains from the Discovery sample. Foil1 (**Fig. 4a**) contains
116 an elongated inclusion of $\sim 1.5 \mu\text{m} \times 0.5 \mu\text{m}$ in size, the TEM image of the inclusion shows that an
117 amorphous silica phase fills the inclusion and NPs are encapsulated within this phase (**Fig. 4b**). The
118 NPs form single sub-rounded crystals with diameters that varies from 5 to 8 nm. The absence of
119 atomic arrangement in the silica is confirmed by FFT diffractogram. The EDS map acquired from the
120 area with the inclusion indicates that the amorphous phase is composed of silica and the four NPs
121 encapsulated in the amorphous silica are composed of Au (supplementary information). The Au NPs
122 composition is further confirmed by the d-spacing of 2.34 \AA (111) obtained from FFT
123 pattern/diffractogram on all the NPs.

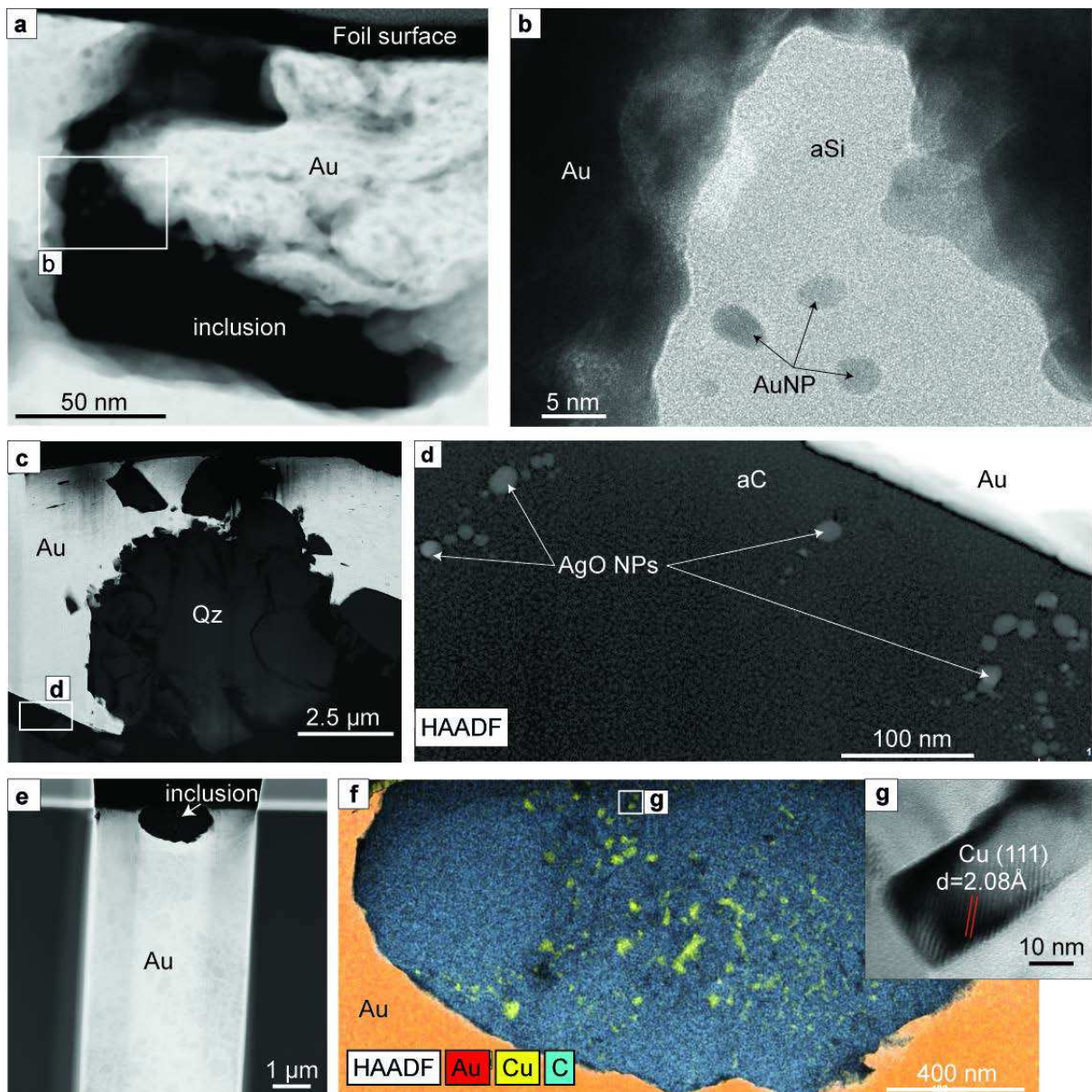
124 The second foil (foil 2) contains quartz fragments, coarse gold and amorphous carbonic phase
125 between the quartz fragments, and the coarse gold (**Fig. 4c**). The composition of each phase in foil 2
126 is confirmed by EDS elemental maps and the crystalline state is confirmed by HRTEM and FFT

127 diffractograms (supplementary information). Within the lower part of foil 2, approximately 20 NPs
 128 were identified within the amorphous carbonic phase (**Fig. 4d**), EDS spectra acquired from the NPs
 129 indicate a compositional phase that includes Ag and O which is confirmed by a d-spacings of 2.78Å
 130 (11-1) and 1.59Å (31-2) calculated from a FFT diffractogram that corresponds to AgO structure. The
 131 AgO NPs diameter varies from 8 to15 µm.



132
 133 **Fig. 3: Beta Hunt nanoparticles in amorphous carbon and silica.** **a.** STEM image of the entire Beta Hunt foil
 134 showing a large inclusion on the left-hand side and a smaller inclusion on the right-hand side of the foil; **b.** EDS
 135 element map of part of the larger inclusion indicated in a white rectangle in Fig. 3a. showing the presence of
 136 silica in the centre of the inclusion and a thin layer of carbon along the contact with gold; **c.** TEM image of the
 137 area shown in a white rectangle in Fig. 3b. The image shows amorphous silica (aSi) in the right-side of the
 138 image, amorphous carbon (aC) is concentrated along the contact between the amorphous silica and the host
 139 gold crystal, numerous rounded Au or Ag NPs (Au NP) are encapsulated in the amorphous carbon phase. **d.**
 140 HRTEM image of the area indicated by a white rectangle in Fig. 3c. showing one Au (or Ag) NP in amorphous
 141 carbon that is between 3 and 5 nm in diameter. One diffractogram was acquired over the Au (or Ag) NP that
 142 confirms a d-spacing of 2.37Å for the NP.

143



144

145 **Fig. 4: Gold, silver oxide and copper nanoparticles in amorphous carbon and silica.** **a.** STEM image of the
 146 inclusion in Discovery sample foil 1; **b.** TEM image of the area indicated by a white rectangle in Fig. 4a that
 147 shows the amorphous silica phase filling the inclusion and rounded Au NP floating within the amorphous phase;
 148 **c.** Backscatter electron image of Discovery foil 2, the lighter grey crystalline phase corresponds to coarse gold
 149 (Au), the dark grey phase corresponds to quartz (Qz) and the black phase within the foil is composed of
 150 amorphous carbonic material; **d.** HAADF image of the area indicated by a white rectangle in Fig. 4c showing
 151 rounded silver oxide nanoparticles (AgO NP) within the amorphous carbon phase (aC). A diffractogram
 152 acquired over the NP confirms their composition with d -spacing of 2.78\AA for (11-1) and 1.59\AA for (31-2); **e.**
 153 Backscatter electron image of the Sixteen to One foil that shows the inclusion studied at the surface of the foil;
 154 **f.** EDS elemental map of the Sixteen to One inclusion showing that it is mainly composed of carbon with minor
 155 NPs of copper interstitial to the carbon micro-crystals; **g.** HRTEM image of the area indicated by a rectangle in
 156 Fig. 4f that shows a Cu NP of 30 nm large and 50 nm long with a d -spacing of 2.08\AA that confirms the copper
 157 composition of the NP.

158

159 **Callie.** The observations reported from the Callie TEM foil have been extended from Petrella, et al.
160 ¹⁵. Petrella, et al. ¹⁵ reported the presence of Au NP preserved in amorphous silica present in an
161 inclusion in coarse gold from a quartz vein. In this study we acquired an EDS elemental map of the
162 same entire inclusion whereas Petrella, et al. ¹⁵ study was only focused on the area that contains the
163 Au NPs. The elemental map acquired in this study (supplementary information) revealed that only
164 the left side of the inclusion is composed of amorphous silica whereas the rest of the inclusion is
165 composed of an amorphous carbonic phase.

166 **Sixteen to One.** One foil (**Fig. 4e**) was extracted from the Discovery sample, in a coarse gold grain,
167 bearing numerous carbon-rich inclusions < 3 µm. The foil contains a 2 µm large sub-rounded
168 inclusion, mainly composed of crystalline micro-grains of carbon which vary in size from
169 approximately 20nm to 100nm (supplementary information). Within the inclusion, there are more
170 than 20 NPs composed of copper that are interstitial to the crystalline carbon (**Fig. 4f**). The
171 composition of the NPs was confirmed using EDS and FFT patterns/diffractograms that show a d-
172 spacing of 2.08Å that corresponds to native copper (**Fig. 4g**). The Cu NPs are rather large with sizes
173 varying from 10 nm to 100 nm and are not rounded but rather display sub-angular shapes.

174

175 ***Dominant phase chemistry of Gold micro-inclusions***

176 The composition of the amorphous phases associated to the NPs was acquired using EDS on the TEM
177 (further information is provided in supplementary information).

178 **An amorphous silica phase** was identified in inclusions in gold grains from the Beta Hunt, the
179 Discovery and the Callie samples. Measured amorphous silica composition in all the sample includes
180 Si (varies from ~38 At% to ~56 At%), O (varies from ~44 At% to ~62 At%) and minor or trace amount
181 of gold (< 1.5 At%).

182 **An amorphous carbonic phase** was identified in inclusions in gold grains from the Beta Hunt, the
183 Discovery, the Red Lake and the Callie samples. The result for the amorphous carbonic phase
184 composition reveals that the phase systematically contains C (varies from ~70 At% to ~93 At%), O

185 (varies from ~4 At% to ~19 At%) and N (varies from ~1 At% to ~3 At%) with minor or trace amount of
186 gold (< 1 At%).

187

188 Discussion

189 The transport of Au, and metals in crustal aqueous solutions is generally assumed to be as dissolved
190 hydrosulfide aqueous species²⁹. However, observations of gold NP in orogenic gold systems
191 challenge this assumption^{15,16}. By reporting the occurrence of metal NPs in five orogenic gold
192 deposits, our study demonstrates that metal NPs are ubiquitous in orogenic gold deposits.

193 Moreover, it confirms that a change of paradigm is required to better understand how NPs
194 contribute to the broader metal endowment. The intimate and systematic association between
195 carbon- and amorphous silica-bearing phases with metals NPs is reported for the first time in this
196 study. It provides insights into the processes allowing for metal transfer and formation of high-grade
197 metalliferous deposits.

198 In this study, we also show the presence of AgO, AgAu and Cu NPs, suggesting that these metals can
199 also occur as NPs in hydrothermal solutions. It is assumed that the processes leading to the
200 nucleation of Au NPs may also apply to Ag and Cu NPs. At the conditions of orogenic gold deposit
201 formation, experiments show that Ag and Cu, unlike Au, tend to preferentially form complexes with

202 chlorine rather than with reduced sulfur. Consequently, Cu(I) is most likely stable as CuCl₂⁻³⁰ and
203 Ag(I) as AgCl₂⁻³¹. However, these metal-chlorine complexes have stability fields that differ from that
204 of Au-hydrosulfide complexes at the pressure and temperature conditions of interest³¹⁻³⁴.

205 Therefore, co-destabilisation of Au, Ag and Cu-bearing complexes and concomitant nucleation of Au,
206 Ag and Cu NPs are unlikely to occur at the site of mineralisation. As an alternative, the coexistence of
207 Au, Ag and Cu NPs in gold deposits supports a model whereby nucleation of metal NPs occurs away
208 from the site of deposition.

209 In a recent study, McLeish, et al.³⁵ propose that nucleation of electrum occurs in the upper levels of
210 the porphyry environment that provides the conditions necessary for Au supersaturation. A deeper

211 equivalent of such system can be envisioned as a potential nucleation source for the NPs present in
212 our samples. In their model, McLeish, et al.³⁵ suggest that colloidal transport is made possible by a
213 system that is maintained in a nonequilibrium state (e.g. boiling) arguing that both nucleation rates
214 (high) and growth rates (low) would preclude the NPs growth and crystal formation. Such model can
215 explain the nucleation and transport over short distances in the vicinity of the mineralisation site in a
216 porphyry or epithermal environment. It remains difficult to understand how the proposed model
217 may apply to orogenic systems which are hosted in mid- to upper-crustal levels and formed far from
218 their deep-seated fluid and metal source^{4,5}. The range of formation depth of the orogenic gold
219 deposits studied in this contribution (1.5 to > 5 km deep) indicates potential colloidal transport over
220 several kilometers. It is unlikely that metal supersaturation as described by McLeish, et al.³⁵ can be
221 maintained over such a distance.

222 The observation that some NPs reported in this study are as small as 1nm and that a majority are
223 <10nm in diameter indicates that colloidal stabilisation was reached soon after the NPs nucleation,
224 with limited growth by coalescence or Ostwald Ripening³⁶. In the case of orogenic gold
225 mineralisation, stabilisation may have occurred by the adsorption of colloidal silica onto metal NPs
226^{14,37} that acted as an efficient aggregation barrier that prevented the continuous growth of the NPs
227 and complete deposition of the metal out of solution. Such a hypothesis is further supported by the
228 intimate and quasi systematic association of amorphous silica with metal NPs observed in this study.

229 Regardless of the age, nature of the host rocks or depth of the deposit, our data indicate that the
230 stabilisation of metal NPs by colloidal silica is likely to occur in natural systems.

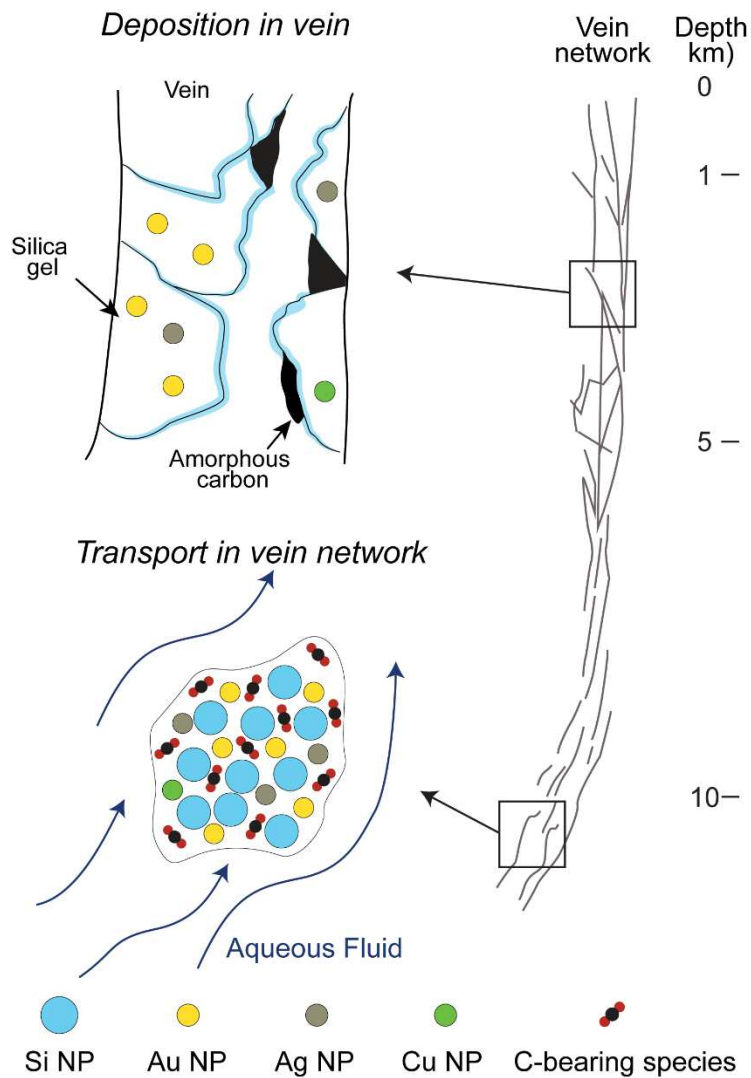
231 Another crucial outcome of this study is the novel documentation of the systematic association of
232 metals NPs with amorphous or micro-crystalline carbon. The amorphous carbonic phase observed in
233 all but one deposit is always composed of C, O and N which are the same elements that are found in
234 carbon-rich fluid inclusions that are commonly found in orogenic gold deposits³⁸⁻⁴⁰. The composition
235 of the fluid inclusions in orogenic gold deposits is generally dominated by CO₂ with minor CH₄ and N₂
236⁴⁰. The comparable elemental composition observed between the amorphous carbonic phases

237 documented in this study and fluid inclusions from orogenic deposits suggests that the amorphous
238 material has originated from the media transporting the metals, as opposed to derived from the
239 host rocks to the deposit. This is further supported by the observation that the deposits investigated
240 are hosted in various rock types; some of which have carbon-poor compositions (i.e. basalt; SI). The
241 components of the amorphous carbonic inclusions might therefore derive from CO₂, CH₄ and minor
242 N₂ that were initially present in the fluid as gaseous or supercritical phases.

243 We put forward the hypothesis that the textural observations presented in our study reflect a
244 previously unrecognized process that plays a role in the stabilisation of NP in aqueous solution and
245 facilitate their migration through vein systems in the upper crust. The transport of metal NPs may
246 have been facilitated across the mid-crust (10 to 1 km deep) by the combined contributions of silica
247 and gaseous/supercritical phases such as CO₂, CH₄ and N₂ under the form of nanoparticle emulsion.
248 Within such emulsion, the amorphous silica acts as an interparticle barrier that prevents the
249 aggregation of metal NPs but increases the density of NPs. The density rise is counterbalanced by
250 the contribution of the gaseous/supercritical phases that provides the buoyancy and low viscosity
251 required to allow for the physical transport of the of nanoparticle emulsion in the upper 10 km of
252 the Earth's crust (**Fig. 5**). A similar process was previously proposed ⁴¹ involving supercritical CO₂ as a
253 driving force to facilitate the transport of ascending metal bearing dense sulfide liquids in silicate
254 melts in the lower crust.

255 The nanoparticle emulsions are subsequently destabilised at the site of mineralisation by processes
256 such as pressure reduction or fluid-rock interaction depending on the deposit ⁶. Fluid phase
257 separation at the site of deposition, for example, can increase the collision rate between NP and
258 cause their aggregation ^{12,42-45}. Alternatively, fluid-rock interaction might locally change the
259 thermochemical conditions of the solution leading to destabilisation of Au-silica colloidal complexes
260 and triggers aggregation of NPs and gold deposition in veins. Destabilisation of colloidal emulsion at
261 the site of deposition may have also caused precipitation of the amorphous carbonic phase ⁴⁶, which
262 may also be responsible for the destabilisation and deposition of amorphous silica containing the

263 metal NPs. With time, the amorphous silica crystallized into quartz which expelled the gold NPs
 264 outside of the crystalline structure followed by their amalgamation into coarse gold grains^{13,15}.
 265 The model presented in this study changes the current understanding of metal transport within
 266 crustal hydrothermal systems. It represents a paradigm shift that impacts our understanding of how
 267 gold orebodies form but, more generally, this model also impacts our broader understanding of
 268 metal transfer in the Earth's crust.



269
 270 **Fig. 5: Proposed model for the transport of metal NPs in the Earth's upper crust in the form of a nanoparticle**
 271 **emulsion.** The nanoparticle emulsion is composed of metal NPs, colloidal silica and low-density carbonic fluid.
 272 The colloidal silica prevents the aggregation of the metal NP and the carbonic phase provides buoyancy to the
 273 emulsion. Upon destabilisation at the site of mineralisation, the carbonic phase is precipitated under the form
 274 of amorphous carbon and the colloidal silica is precipitated under the form of amorphous silica in veins. Both
 275 amorphous phases encapsulate metal nanoparticles upon deposition, some of which were preserved in
 276 inclusions.

277

278 **Method**

279 ***Sample selection***

280 Five hand-samples of gold-rich quartz veins were obtained from five gold deposits which are
281 characterized by locally high-grade (with abundant visible gold; ¹⁷) deposits that formed at crustal
282 depths ranging from >5 km to 1.5 km deep (**Fig. 1**). The deposits formed in different host rocks and
283 ages ranging from the Archean to the Cretaceous (**Fig. 1**). Details on the age of formation, pressure
284 and temperature conditions of mineralisation emplacement, petrology and host-rocks of the
285 deposits are summarized in SI.

286 ***Sample preparation***

287 For each sample, a small piece of approximately 2cm x 2cm containing coarse gold was cut and
288 embedded in a one-inch epoxy mount. The sample preparation was designed to avoid surface
289 contamination by Si and C as much as possible. The mounts were first mechanically ground (1200
290 grit) using AlO abrasive and then polished in three successive steps (9, 3, and 1 µm) with medium
291 diamond polishing compounds. It is worth noting that carbon with diamond crystalline structure as
292 used for fine polishing cannot be mistaken with amorphous carbon phases with the analytical
293 techniques used in this study. The mounts were subsequently coated with platinum for SEM
294 investigations.

295 ***Petrographic characterisation***

296 All the analytical work was completed at the Centre for Microscopy, Characterisation and Analysis
297 (CMCA) at the University of Western Australia.

298 Petrographic imaging and elemental analysis of the mounts were carried out using a Verios XHR SEM
299 equipped with an Oxford Instrument 80mm2 X-max SDD EDS detector. This step was followed by the
300 extraction of ultrathin TEM samples (foils) of approximately 10 x 10 x 0.1 µm, designed to investigate
301 the microscopic inclusions within the gold grains using a dual-beam FIB-SEM system (FEI Helios
302 NanoLab G3 CX). Electron beam imaging within the dual-beam FIB was used to identify previously
303 mapped areas of interest in the mounts allowing site-specific TEM samples to be prepared. The TEM

304 sections were prepared through a series of steps involving different ion beam energies (2-30kV) and
305 currents (40pA-21nA). After initial thinning to ~1 µm the foils were extracted using an in-situ
306 Tungsten micromanipulator and welded onto PELCO FIB-lift-out Cu TEM grids. Final thinning to ~ 100
307 nm was then achieved on the grid using lower beam currents.
308 The TEM sections were then analysed using a FEI Titan G2 80-200 TEM/STEM with ChemiSTEM
309 Technology operating at 200 kV. High Resolution imaging, High Angle Annular Dark Field Scanning
310 Transmission Electron Microscopy (HAADF-STEM) imaging and Energy-dispersive X-ray spectroscopy
311 elemental mapping were carried out to obtain structural and compositional information from the
312 samples. EDS quantitative measurements were performed using Bruker Esprit software.
313 Details on the areas selected for each measurement is provided in SI.

314

315 **References**

- 316 1 Kenny, S. L. & Venable, S. L. *Gold: a cultural encyclopedia*. (ABC-CLIO, 2011).
317 2 Evans, K. A. & Tomkins, A. G. Metamorphic fluids in orogenic settings. *Elements: An
318 International Magazine of Mineralogy, Geochemistry, and Petrology* **16**, 381-387 (2020).
319 3 Phillips, G. N. in *Proceedings of World Gold*. 15-21.
320 4 Goldfarb, R. J. & Groves, D. I. Orogenic gold: common or evolving fluid and metal sources
321 through time. *Lithos* **233**, 2-26 (2015).
322 5 Phillips, G. N. & Powell, R. Formation of gold deposits: a metamorphic devolatilization
323 model. *Journal of Metamorphic Geology* **28**, 689-718, doi:10.1111/j.1525-1314.2010.00887.x
324 (2010).
325 6 McCuaig, T. C. & Kerrich, R. P—T—t—deformation—fluid characteristics of lode gold
326 deposits: evidence from alteration systematics. *Ore Geology Reviews* **12**, 381-453 (1998).
327 7 Pokrovski, G. S., Akinfiev, N. N., Borisova, A. Y., Zotov, A. V. & Kouzmanov, K. Gold speciation
328 and transport in geological fluids: insights from experiments and physical-chemical
329 modelling. *Geol Soc Spec Publ* **402**, 9-70, doi:10.1144/Sp402.4 (2014).
330 8 Petrella, L. et al. Contemporaneous formation of vein-hosted and stratabound gold
331 mineralization at the world-class Dead Bullock Soak mining camp, Australia. *Mineralium
332 Deposita* **55**, 845-862, doi:10.1007/s00126-019-00902-7 (2020).
333 9 Williams-Jones, A. E., Bowell, R. J. & Migdisov, A. A. Gold in solution. *Elements* **5**, 281-287
334 (2009).
335 10 Pearce, M. A., White, A. J., Fisher, L. A., Hough, R. M. & Cleverley, J. S. Gold deposition
336 caused by carbonation of biotite during late-stage fluid flow. *Lithos* **239**, 114-127 (2015).
337 11 Lindgren, W. Geology and mineral deposits of the National mining district, Nevada.
338 (Washington: Government Printing Office, 1915).
339 12 Saunders, J. A. Colloidal transport of gold and silica in epithermal precious-metal systems:
340 Evidence from the Sleeper deposit, Nevada. *Geology* **18**, 757-760 (1990).
341 13 Herrington, R. J. & Wilkinson, J. J. Colloidal Gold and Silica in Mesothermal Vein Systems.
342 *Geology* **21**, 539-542, doi:Doi 10.1130/0091-7613(1993)021<0539:Cgasim>2.3.Co;2 (1993).

- 343 14 Liu, W. *et al.* Colloidal gold in sulphur and citrate-bearing hydrothermal fluids: An
344 experimental study. *Ore Geology Reviews* **114**, 103142 (2019).
- 345 15 Petrella, L. *et al.* Colloidal gold transport: a key to high-grade gold mineralization?
346 *Mineralium Deposita*, 1-8 (2020).
- 347 16 Voisey, C. R. *et al.* Aseismic Refinement of Orogenic Gold Systems. *Economic Geology* **115**,
348 33-50 (2020).
- 349 17 Twomey, T. & McGibbon, S. The geological setting and estimation of gold grade of the high-
350 grade zone, Red Lake mine, Goldcorp Inc. *Exploration and Mining Geology* **10**, 19-34 (2001).
- 351 18 Chi, G., Dubé, B. & Williamson, K. *Fluid evolution and pressure regimes in the Campbell-Red*
352 *Lake gold deposit, Red Lake mine trend, Red Lake, Ontario: Fluid-inclusion evidence for a*
353 *protracted, highly dynamic hydrothermal system.* (Natural Resources Canada, Geological
354 Survey of Canada, 2003).
- 355 19 Neall, F. B. & Phillips, G. N. Fluid-wall rock interaction in an Archean hydrothermal gold
356 deposit; a thermodynamic model for the Hunt Mine, Kambalda. *Economic Geology* **82**, 1679-
357 1694 (1987).
- 358 20 Shelton, K. L., McMenamy, T. A., Hees, E. H. P. v. & Falck, H. Deciphering the Complex Fluid
359 History of a Greenstone-Hosted Gold Deposit: Fluid Inclusion and Stable Isotope Studies of
360 the Giant Mine, Yellowknife, Northwest Territories, Canada. *Economic Geology* **99**, 1643-
361 1663, doi:10.2113/gsecongeo.99.8.1643 (2004).
- 362 21 Coveney, R. M. Gold quartz veins and auriferous granite at the Oriental Mine, Alleghany
363 District, California. *Economic Geology* **76**, 2176-2199 (1981).
- 364 22 Mernagh, T. P. & Wygralak, A. S. Gold ore-forming fluids of the Tanami region, Northern
365 Australia. *Mineralium Deposita* **42**, 145-173, doi:10.1007/s00126-006-0098-y (2007).
- 366 23 Dubé, B. *et al.* Timing of gold mineralization at Red Lake, northwestern Ontario, Canada:
367 New constraints from U-Pb geochronology at the Goldcorp high-grade zone, Red Lake Mine,
368 and the Madsen Mine. *Economic Geology* **99**, 1611-1641 (2004).
- 369 24 Thébaud, N. *et al.* Protracted and polyphased gold mineralisation in the Agnew District
370 (Yilgarn Craton, Western Australia). *Precambrian Research* **310**, 291-304,
371 doi:10.1016/j.precamres.2018.02.013 (2018).
- 372 25 Vielreicher, N., Groves, D., McNaughton, N. & Fletcher, I. The timing of gold mineralization
373 across the eastern Yilgarn craton using U-Pb geochronology of hydrothermal phosphate
374 minerals. *Mineralium Deposita* **50**, 391-428, doi:10.1007/s00126-015-0589-9 (2015).
- 375 26 Ootes, L. *et al.* The timing of Yellowknife gold mineralization: A temporal relationship with
376 crustal anatexis? *Economic Geology* **106**, 713-720 (2011).
- 377 27 Marsh, E. E. *et al.* New constraints on the timing of gold formation in the Sierra Foothills
378 province, central California. *Ores and orogenesis: Circum-Pacific tectonics, geologic*
379 *evolution, and ore deposits: Arizona Geological Society Digest* **22**, 369-388 (2008).
- 380 28 USGS. (USGS Earthquake Hazards Program, USGS Website, 2012).
- 381 29 Seward, T. M., Williams-Jones, A. E. & Migdisov, A. A. in *Treatise on Geochemistry* Vol. 13
382 29-57 (2014).
- 383 30 Brugger, J. *et al.* An XAS study of the structure and thermodynamics of Cu(I) chloride
384 complexes in brines up to high temperature (400°C, 600bar). *Geochimica et Cosmochimica
385 Acta* **71**, 4920-4941, doi:<https://doi.org/10.1016/j.gca.2007.08.003> (2007).
- 386 31 Pokrovski, G. S. *et al.* Silver in geological fluids from in situ X-ray absorption spectroscopy
387 and first-principles molecular dynamics. *Geochimica et Cosmochimica Acta* **106**, 501-523,
388 doi:<https://doi.org/10.1016/j.gca.2012.12.012> (2013).
- 389 32 Akinfiev, N. & Zotov, A. Thermodynamic Description of Chloride, Hydrosulfide, and Hydroxo
390 Complexes of Ag (I), Cu (I), and Au (I) at Temperatures of 25-500°C and Pressures of 1-
391 2000 bar. *GEOCHEMISTRY INTERNATIONAL C/C OF GEOKHIMIIA* **39**, 990-1006 (2001).

- 392 33 Stefánsson, A. & Seward, T. Experimental determination of the stability and stoichiometry of
393 sulphide complexes of silver (I) in hydrothermal solutions to 400 C. *Geochimica et*
394 *Cosmochimica Acta* **67**, 1395-1413 (2003).
- 395 34 Etschmann, B. *et al.* An in situ XAS study of copper (I) transport as hydrosulfide complexes in
396 hydrothermal solutions (25–592 C, 180–600 bar): speciation and solubility in vapor and
397 liquid phases. *Geochimica et Cosmochimica Acta* **74**, 4723-4739 (2010).
- 398 35 McLeish, D. F., Williams-Jones, A. E., Vasyukova, O. V., Clark, J. R. & Board, W. S. Colloidal
399 transport and flocculation are the cause of the hyperenrichment of gold in nature.
400 *Proceedings of the National Academy of Sciences* **118**, e2100689118,
401 doi:10.1073/pnas.2100689118 (2021).
- 402 36 Polte, J. Fundamental growth principles of colloidal metal nanoparticles—a new perspective.
403 *CrystEngComm* **17**, 6809-6830 (2015).
- 404 37 Frondel, C. Stability of colloidal gold under hydrothermal conditions. *Economic Geology* **33**,
405 1-20 (1938).
- 406 38 Diamond, L. W. Fluid chemistry of orogenic lode gold deposits and implications for genetic
407 models. *Gold in 2000* **13**, 141 (2000).
- 408 39 Van den Kerkhof, A. & Thiery, R. Carbonic inclusions. *Lithos* **55**, 49-68 (2001).
- 409 40 Chi, G., Dubé, B., Williamson, K. & Williams-Jones, A. E. Formation of the Campbell-Red Lake
410 gold deposit by H₂O-poor, CO₂-dominated fluids. *Mineralium Deposita* **40**, 726 (2006).
- 411 41 Blanks, D. E. *et al.* Fluxing of mantle carbon as a physical agent for metallogenic fertilization
412 of the crust. *Nature Communications* **11**, 1-11 (2020).
- 413 42 Gartman, A. *et al.* Boiling-induced formation of colloidal gold in black smoker hydrothermal
414 fluids. *Geology* **46**, 39-42 (2018).
- 415 43 Hannington, M., Harðardóttir, V., Garbe-Schönberg, D. & Brown, K. L. Gold enrichment in
416 active geothermal systems by accumulating colloidal suspensions. *Nature Geoscience* **9**, 299
417 (2016).
- 418 44 Saunders, J. A., Burke, M. & Brueseke, M. E. Scanning-electron-microscope imaging of gold
419 (electrum) nanoparticles in middle Miocene bonanza epithermal ores from northern
420 Nevada, USA. *Mineralium Deposita* **55**, 389-398 (2020).
- 421 45 Saunders, J. A. Silica and gold textures in bonanza ores of the Sleeper Deposit, Humboldt
422 County, Nevada; evidence for colloids and implications for epithermal ore-forming
423 processes. *Economic Geology* **89**, 628-638 (1994).
- 424 46 Hu, S.-Y., Evans, K., Craw, D., Rempel, K. & Grice, K. Resolving the role of carbonaceous
425 material in gold precipitation in metasediment-hosted orogenic gold deposits. *Geology* **45**,
426 167-170 (2017).
- 427

428 Acknowledgments

429 This project was funded internally within the University of Western Australia. N.T. acknowledges the
430 Hammond and Nisbet fellowship. D.F. acknowledges ARC funding DE190101307.

431

432 **Authors contributions**

433 L.P. and N.T. designed the study. S.T. collected the samples and field observations. L.P. prepared the
434 samples and conducted the analyses. A.S. and S.G. provided guidance and support with sample
435 preparation and analyses. L.P., N.T., D.F., L.M., S.T., A.S., S.G. wrote the manuscript.

436

437 **Competing interests**

438 The authors declare no competing interests.

439

440 **Corresponding author**

441 Correspondence to Laura Petrella laura.petrella@uwa.edu.au.

442

443 **Figure legends**

444 **Fig. 1: Sample's location and description.** **a.** Location of the deposits from which samples were
445 collected for this study; the deposit locations are shown on a world map indicating the thermo-
446 tectonic age of the country rocks, modified from USGS thermo-tectonic data ²⁸. **b** to **f** show
447 photographs of the gold-rich quartz vein specimen used in this study: **b.** Discovery sample; **c.** Sixteen
448 to One sample; **d.** Red Lake sample; **e.** Beta Hunt sample; **f.** Callie sample. **g.** Schematic
449 representation showing the variability in depth of formation for the deposits studied along a crustal-
450 scale network of fractures and faults.

451 **Fig. 2: Red Lake electrum nanoparticles in amorphous carbon.** **a.** TEM image of the Red Lake foil
452 showing the elongated inclusion at the surface of the foil that is mainly composed of quartz (Qz) and
453 an amorphous carbonic-phase (aC), the rest of the foil comprises coarse gold including two grains of
454 different crystal orientation, the foil is covered by a platinum (Pt) protective layer at the top of the
455 foil; **b.** EDS element map overlaying a High-Angle Annular Dark Field (HAADF) image from the middle

456 of the inclusion and indicated in a white rectangle in Fig 2a. The figure shows the presence of
457 electrum NP encapsulated in a carbon-rich phase; **c.** TEM image of the area shown in a white
458 rectangle in Fig 2a. The inclusion is composed of amorphous material that is mainly carbon (light
459 grey) and NPs that are the darker grey sub-rounded features within the amorphous material. The
460 two large, "bubble"-like features in the image correspond to cavities within the amorphous phase,
461 the cavities may have formed during the thinning of the foil. The absence of atomic arrangement
462 within the carbon phase was confirmed by a diffractogram obtained in the lower part of the image
463 avoiding the NP; **d and e.** High Resolution TEM (HRTEM) image of the areas shown in black
464 rectangles in Fig 2c. showing electrum NPs with sizes varying between 4 nm to 10 nm in diameter.
465 The diffractogram collected over the largest NP confirms a d-spacing of 2.34 that corresponds to Ag
466 and/or Au.

467 **Fig. 3: Beta Hunt nanoparticles in amorphous carbon and silica.** **a.** STEM image of the entire Beta
468 Hunt foil showing a large inclusion on the left-hand side and a smaller inclusion on the right-hand
469 side of the foil; **b.** EDS element map of part of the larger inclusion indicated in a white rectangle in
470 Fig. 3a. showing the presence of silica in the centre of the inclusion and a thin layer of carbon along
471 the contact with gold; **c.** TEM image of the area shown in a white rectangle in Fig. 3b. The image
472 shows amorphous silica (aSi) in the right-side of the image, amorphous carbon (aC) is concentrated
473 along the contact between the amorphous silica and the host gold crystal, numerous rounded Au or
474 Ag NPs (Au NP) are encapsulated in the amorphous carbon phase. **d.** HRTEM image of the area
475 indicated by a white rectangle in Fig. 3c. showing one Au (or Ag) NP in amorphous carbon that is
476 between 3 and 5 nm in diameter. One diffractogram was acquired over the Au (or Ag) NP that
477 confirms a d-spacing of 2.37 \AA for the NP.

478 **Fig. 4: Gold, silver oxide and copper nanoparticles in amorphous carbon and silica.** **a.** STEM image
479 of the inclusion in Discovery sample foil 1; **b.** TEM image of the area indicated by a white rectangle in
480 Fig. 4a that shows the amorphous silica phase filling the inclusion and rounded Au NP floating within
481 the amorphous phase; **c.** Backscatter electron image of Discovery foil 2, the lighter grey crystalline

482 phase corresponds to coarse gold (Au), the dark grey phase corresponds to quartz (Qz) and the black
483 phase within the foil is composed of amorphous carbonic material; **d.** HAADF image of the area
484 indicated by a white rectangle in Fig. 4c showing rounded silver oxide nanoparticles (AgO NP) within
485 the amorphous carbon phase (aC). A diffractogram acquired over the NP confirms their composition
486 with d-spacing of 2.78Å for (11-1) and 1.59Å for (31-2); **e.** Backscatter electron image of the Sixteen
487 to One foil that shows the inclusion studied at the surface of the foil; **f.** EDS elemental map of the
488 Sixteen to One inclusion showing that it is mainly composed of carbon with minor NPs of copper
489 interstitial to the carbon micro-crystals; **g.** HRTEM image of the area indicated by a rectangle in Fig.
490 4f that shows a Cu NP of 30 nm large and 50 nm long with a d-spacing of 2.08Å that confirms the
491 copper composition of the NP.

492 **Fig. 5: Proposed model for the transport of metal NPs in the Earth's upper crust in the form of a**
493 **nanoparticle emulsion.** The nanoparticle emulsion is composed of metal NPs, colloidal silica and
494 low-density carbonic fluid. The colloidal silica prevents the aggregation of the metal NP and the
495 carbonic phase provides buoyancy to the emulsion. Upon destabilisation at the site of
496 mineralisation, the carbonic phase is precipitated under the form of amorphous carbon and the
497 colloidal silica is precipitated under the form of amorphous silica in veins. Both amorphous phases
498 encapsulate metal nanoparticles upon deposition, some of which were preserved in inclusions.

Supplementary Files

This is a list of supplementary files associated with this preprint. Click to download.

- [SupplementaryInformation.pdf](#)